Influence of graphene oxide lateral size on the properties and performances of forward osmosis membrane

Nawshad Akther[a], Ziwen Yuan[b], Yuan Chen[b], Sungil Lim[a], Sherub Phuntsho[a], Noreddine Ghaffour[c], Hideto Matsuyama[d] and Hokyong Shon[a]*

[a] School of Civil and Environmental Engineering, University of Technology Sydney (UTS), NSW 2007, Australia

[b] School of Chemical and Biomolecular Engineering, The University of Sydney, NSW 2006, Australia

[c] King Abdullah University of Science and Technology (KAUST), Water Desalination and Reuse Center (WDRC), Biological & Environmental Science & Engineering Division (BESE), Thuwal, 23955-6900, Saudi Arabia

[d] Research Center for Membrane and Film Technology, Department of Chemical Science and Engineering, Kobe University, 1-1 Rokkodaicho, Nada-ku, Kobe 657-8501, Japan

[*] Corresponding author: Prof. Hokyong Shon Email: hokyong.shon-1@uts.edu.au; Tel.: +61 2 9514 2629; Fax: +61 2 9514 2633.

Keywords: forward osmosis (FO); graphene oxide (GO); lateral size, thin-film nanocomposite (TFN) membrane; interfacial polymerization (IP)

Abstract

Graphene oxide (GO) has been widely explored for the improvement of thin-film composite (TFC) membrane performance. However, the influences of GO flake lateral size on the polyamide (PA) TFC membrane properties and performances have not been investigated. In this study, GO suspensions with an average flake size ranging from 0.01 to 1.06 μm^2 were prepared by varying the sonication duration between 0 to 8 h. The different sized GO flakes were embedded in the PA layer to examine the effect of their size on the morphology and performances of TFC forward osmosis (FO) membranes. The specific reverse solute flux and water flux of the GO-modified thin-film nanocomposite (TFN) membranes improved by over 60% and 50%, respectively, when the average GO flake size was reduced from 1.06 to 0.01 μm^2 due to the formation of a thinner and more uniform PA layer. Large GO flakes deteriorated membrane performance by creating impervious regions that obstructed the reaction between monomers during the interfacial polymerization process resulting in defective PA layer formation. Whereas, smaller GO flakes distributed more uniformly in the PA layer creating fewer defects, and demonstrated better desalination performance and antifouling property than the TFN membranes modified with larger GO flakes. These results deliver strategies for future improvements in GO or 2D nanomaterial-based TFN membranes, where smaller flake size can be beneficial for minimizing PA layer defects.

1. Introduction

Extensive studies have been conducted on osmotically-driven membrane processes like forward osmosis (FO) and pressure-retarded osmosis (PRO) for power generation [1], desalination [2-4], resource recovery [5], wastewater treatment [6], brine or seawater dilution [7, 8], osmotic membrane bioreactors [9], concentration of aqueous products like fruit juice [10] and dairy whey [11]. The difference in osmotic potential between the draw solution (DS) and feed solution (FS) mainly drives the water through the semi-permeable membrane in FO processes without the need for hydraulic pressure [12]. As a result, these processes are associated with many desirable characteristics like (1) potential for high water recovery, (2) desirable rejection of numerous contaminants, (3) low fouling tendency, and (3) possibly less energy consumption depending on the type of application [13].

The fabrication of robust and highly selective osmotic membranes is amongst the most critical research areas in the field of engineered osmotic processes. A standard FO membrane should demonstrate low structural parameter, high solute rejection and water permeability, excellent anti-fouling property, good chemical resistance and mechanical strength [14]. Numerous works have been done on polyamide (PA) based thin-film composite (TFC) membranes compared to other asymmetric membranes, such as cellulose triacetate, as they demonstrate much higher water permeability combined with superior selectivity over a wide pH range [15]. However, TFC membranes can be highly susceptible to fouling, especially during their long-term operations, with very poor resistance to chlorine exposure. Thus, several researchers have tried to heighten the antifouling and antibacterial properties of the TFC membrane by modifying the membrane surface, such as by coating or embedding nanomaterials like graphene oxide (GO), silver, metal-organic

65 frameworks (MOF) and carbon nanotubes, to develop thin-film nanocomposite (TFN) membranes
66 [14, 16-20].
67
68 Over the last few years, GO has drawn researchers' attention because of their distinct structure,
69 hydrophilicity, superior antibacterial properties, high chemical stability and low production cost
70 [21, 22]. GO flakes are two-dimensional single-atom-thick structures that exhibit exceptional
71 hydrophilic properties owing to the occurrence of oxygen-containing hydroxyl, epoxy and
72 carboxyl groups on their surfaces and edges [23]. GO-modified membranes have been reported to
73 demonstrate improved mechanical strength, thermal stability, water permeability, chlorine
74 resistance and antifouling properties [24-26]. Shen et al. incorporated GO in the PA layer of the
75 TFC membrane, which produced a much smoother and thinner PA layer than the unmodified
76 membrane [27]. They observed that GO-modified TFN membranes reduced sodium alginate
77 fouling by reducing sites on the PA surface for foulant adhesion and electrostatically repelling the
78 alginate molecules. Wu et al. chemically-modified GO with polyvinylpyrrolidone (PVP) to
79 minimize GO accumulation in the polymer matrix and confirmed that GO could enhance the
80 membrane permeability, selectivity and hydrophilicity [28]. Hegab et al. reported that grafting GO
81 nanosheets on PA layer significantly improved the antibacterial property of the modified
82 membranes [29]. The numerous studies published on GO-incorporated membranes proved that
83 membrane modification using GO is a promising approach to augment membrane performance.
84
85 Since 2012, several articles have been published on GO-modified TFN membranes for numerous
86 separation processes like nanofiltration (NF), reverse osmosis (RO) and FO. These studies mainly
87 considered the effect of concentration, nanocomposites, chemical modification and

functionalization of GO on the membrane's antifouling properties and performance [30-32]. For example, Kang et al. modified GO with sulfonic acid to produce sulfonated graphene oxide (SGO). They observed that incorporating 0.3 wt.% of SGO into the PA layer improved the hydrophilicity, surface negative charge, water flux, salt rejection and antifouling properties of the NF membranes. The SGO increased the PA cross-linking degree that helped to increase the water flux without deteriorating membrane selectivity [32].

Interestingly, the physicochemical properties of GO was also found to be strongly influenced by the GO flake size. Chen's group observed that the antibacterial property of GO was dependent on the lateral size of the GO flakes, where larger GO flakes exhibited stronger antibacterial activity than the smaller ones [33]. Large GO flakes were easily able to cover the bacterial cells completely and prevent their proliferation, resulting in the loss of cell viability. However, the smaller GO flakes only attached to the bacterial surfaces without isolating the cells effectively. In another study, nano-GO flakes with a lateral width of few nanometers were observed to be photoluminescent in the visible and infrared regions, making them suitable for live cell imaging and potential material for medical and biological applications [34]. Tayyebi et al. demonstrated that graphene quantum dots (GQD) produced from the fragmentation of GO at supercritical condition could enhance the thermal conductivity, absorption coefficient and temperature uniformity of GQD-treated tissues compared to GO flakes, which supported their feasibility for photothermal therapeutic treatment applications [35]. However, the influence of GO lateral size on the PA layer morphology and TFN membrane performance is yet to be investigated.

Therefore, the aim of this study is to investigate the effect of GO lateral size on the PA layer formation during the interfacial polymerization (IP) reaction. The effects of different GO lateral

sizes on the membrane morphology, surface properties and desalination performance were explored. The effect of GO size on the antifouling properties of the membranes was also evaluated using sodium alginate and colloidal silica as model foulants. To the best of our knowledge, this work is the first to study in detail the impact of GO flake lateral size on the PA layer development, and the TFN FO membrane properties and performance.

2. Materials and methods

2.1 Chemicals

Monolayer GO dispersion in water was procured from Graphenea (4 mg/mL, particle size <10 μm). Polysulfone pellets (PSf, Udel® P-3500, Solvay) and 1-methyl-2 pyrrolidone (NMP, ≥ 99.5%, Merck) were employed for membrane substrate preparation. M-phenylenediamine flakes (MPD, 99%), 1,3,5-benzenetricarbonyl trichloride (TMC, 98%) and sodium alginate were bought from Sigma-Aldrich. Colloidal silica (40-41 wt.%, particle size: 70-100 nm, ST-ZL, SNOWTEX®) was procured from Nissan Chemical. N-hexane (98.5%, Merck) was used as a TMC solvent. Deionized (DI) water (~18 MΩ/cm, Milli-Q®, Merck) was used to prepare FS and DS. Sodium chloride (NaCl, > 99.7%) from Chem Supply was used as a draw solute.

2.2 Graphene oxide preparation

Commercial GO water suspension was first diluted to 1 mg/mL with DI water and sonicated for 30 min using an ultrasonic bath (Powersonic 405, Hwashin Technology Co.) to obtain uniform GO dispersion, which was called “GO-0”. The GO flake lateral sizes were then reduced by sonicating GO-0 dispersion for 0.5, 4 and 8 h at 120 W using a digital tip sonicator (S-450D, Branson Ultrasonics Corp.) equipped with a 13 mm disruptor horn. The various GO samples

obtained were called “GO-0.5”, “GO-4” and “GO-8” depending on the duration of tip-sonication. The temperature of the GO dispersions was maintained constant throughout the sonication process by using an ice bath, and the tip sonication cooling interval was set to 5 s for every 30 s. The GO dispersions sonicated at various times showed good stability even after three months of storage.

2.3 TFC and TFN membrane fabrication

2.3.1 Polysulfone membrane substrate

The porous PSf substrates were prepared using the phase inversion technique as described elsewhere [36]. Briefly, a homogenous polymer solution was prepared by dissolving 12 wt. % PSf in NMP at 60 °C and stirring at 500 rpm continuously for 24 h. The well-mixed PSf dope solution was then left for degassing overnight at 34 °C.

A flat-sheet casting machine (Elcometer 4340) and a casting blade with a gate height of 120 µm were employed to cast the polymer solution on a glass plate under ambient conditions. The phase inversion process was initiated by immediately immersing the PSf film-coated glass plate in a coagulation bath holding tap water at room temperature. The solidified PSf substrate was then rinsed thoroughly and stored in DI water at 4 °C for at least 24 h to eradicate the residual solvents.

2.3.2 Polyamide active layer

The fabricated substrate was first wetted with DI water and fixed on a rectangular frame. Any remaining water on the substrate surface was then eliminated with a gentle air knife. IP technique was used to create a selective PA layer on the PSf substrate. In short, the substrate was first submerged for 2.5 min in MPD aqueous solution (4.0 wt./v%). Nitrogen was then employed to gently eradicate the surplus MPD from the substrate, which was then immediately immersed for 1 min in TMC/n-hexane organic solution (0.1 wt.%). Next, the membrane was cured at room temperature for 1 min and at 60 °C for 5 min to improve PA crosslinking degree. The TFC FO

membrane was then washed carefully under running DI water for 3 min to eradicate any residual chemical. Lastly, the membranes were immersed in DI water and stored at 4 °C before testing their performance.

GO-modified TFN membranes were fabricated using a similar protocol like TFC membranes. GO flakes were added to the MPD aqueous solution at a loading of 0.01 wt.% and sonicated for 1 h in a bath sonicator to obtain a homogenous dispersion. The subsequent GO/MPD dispersion on the PSf substrate was brought in contact with the organic solution during the IP reaction to produce GO impregnated PA layer. The GO-modified TFN membranes were denoted as "MGO-0", "MGO-0.5", "MGO-4" and "MGO-8" depending on the duration of tip sonication received by the commercial GO dispersion.

2.4 Graphene oxide and membrane characterization

The lateral size and height of GO flakes were analyzed using the atomic force microscopy (AFM, Dimension 3100, Bruker). The samples for AFM study were assembled by dropping 4 μL of GO dispersions (0.1 g/L) on a freshly cleaved mica and spin coating at 2500 rpm for 150 s. The GO films were then air-dried for AFM analysis. Image J software was used to determine the GO lateral size distribution by measuring approximately 200 GO flakes from the AFM images of each sample. The average GO flake size for each sample was determined by dividing the total sampling area by the total number of GO flakes. AFM was also utilized to investigate the membrane morphology and surface roughness with a scan size of 5 μm × 5 μm.

Scanning electron microscope (SEM, Zeiss Supra 55VP) was used to study the cross-sectional and PA layer top surface morphology of all the membranes. Dry membrane samples were soaked in ethanol prior to rupturing them in liquid nitrogen to prepare the cross-section samples for SEM imaging. Subsequently, the samples were attached to stubs using copper tape and sputter-coated

with a 10 nm thick Au/Pd layer before conducting the SEM analysis. The membrane wettability or hydrophilicity was ascertained by assessing the initial water contact angles on the PA surface at room temperature with an optical tensiometer. The contact angles were assessed at 7 random positions for each sample to acquire the average value.

Fourier transform infrared spectroscopy (FTIR) was employed to confirm the successful integration of the GO flakes through surface chemistry analysis of the fabricated membranes at room temperature. The zeta potentials of the membrane surfaces were quantified at room temperature using an electrokinetic analyzer (SurPASSTM 3, Anton Paar) over a pH range of 3 to 10 using an adjustable gap cell of size 20 × 10 mm. The membranes were attached to the sample holder with the gap height fixed to about 100 µm. 1 mM KCl solution was used as the electrolyte, and 0.05 M HCl and NaOH were used to adjust the pH of the electrolyte. The obtained streaming potential was utilized to verify the membrane surface zeta-potential.

2.5 Membrane performance assessment

2.5.1 Membrane performance

The FO performance of fabricated membranes was established with a laboratory-scale FO system. The complete description of the FO system and membrane cell that was utilized is described in our previous work [36]. The FO membrane cell with a membrane area of 15.4 cm^2 and a flow channel depth of 3 mm on each side of the membrane was used. DI water and 0.5 M NaCl were used as FS and DS, respectively. FS and DS were circulated at 12.6 cm/s, and the temperature was maintained at 22 °C during the performance tests. The membrane performance was determined under both AL-FS and AL-DS (active layer facing to FS and DS, respectively) orientations. The FS weight

200 was recorded at a constant interval using a balance to calculate the water flux. The reverse solute
201 flux was calculated from the FS conductivity recorded with a conductivity meter.
202 The water flux (J_w, $Lm^{-2}h^{-1}$) was estimated by Eq. (1), where ΔV_{FS} (L) is the change in FS volume
203 during the FO performance test, A_m is the actual membrane surface area (m^2) and Δt (h) is the
204 duration of the performance test.

$$J_w = \frac{\Delta V_{FS}}{A_m \Delta t} \quad (1)$$

205 The reverse solute flux (J_s, $gm^{-2}h^{-1}$) across the membrane was evaluated using Eq. (2), where ΔC_{FS}
206 (g/L) is the change in the FS concentration after an interval of Δt (h).

$$J_s = \frac{\Delta C_{FS} V_{FS}}{A_m \Delta t} \quad (2)$$

207 The specific reverse solute flux (*SRSF*, g/L), which denotes membrane selectivity, was obtained
208 using Eq. (3).

$$SRSF = \frac{J_s}{J_w} \quad (3)$$

209 *2.5.2 Membrane transport parameters*
210 The pure water and solute permeability coefficients (A and B, respectively) of the membranes
211 were obtained using the 4-step non-linear regression protocol established for the FO membranes
212 by Tiraferri et al. [37]. The FO performance data for all the membranes required by the numerical
213 model were obtained at four different DS concentrations (0.5, 1.0, 1.5, and 2.0 M NaCl).

214 ***2.6 FO membrane fouling evaluation***

215 The fouling tests for all the membranes were operated in the AL-FS configuration using the FO
216 experimental system described in Section 2.5.1. Baseline experiments were first conducted at a
217 cross-flow velocity of 7.6 cm/s with DI water as FS and NaCl as DS to account for the flux decline

from the decrease in the osmotic driving force resulting from DS dilution and FS concentration. NaCl DS ranging between 0.75 M and 2 M were used to obtain an initial water flux ($J_{w,0}$) of ~25 $Lm^{-2}h^{-1}$. The fouling experiments were then operated at a cross-flow velocity of 7.6 cm/s at the same initial baseline flux by introducing 200 mg/L of colloidal silica and sodium alginate into the FS. The flux decline detected in this case occurred due to the cumulative effect of DS dilution, reverse solute diffusion and membrane fouling. The baseline and fouling tests were run until a total permeate volume of 100 mL was collected. After completing the fouling tests, the membranes were physically cleaned for 1 h by circulating DI water in both FS and DS channels at 12.6 cm/s. The recovered water flux was then obtained by using the same conditions as the baseline study.

3. Results and discussion

3.1 Graphene oxide characterization

The lateral size of GO flakes was reduced via high power sonication without undermining their surface chemical properties. The lateral dimensions of GO flakes were up to several micrometers before sonication as shown in Figure 1A; however, increasing the sonication time reduced the average GO flake size to few nanometers as can be observed from Figure 1B to D. This is also evident from the corresponding GO flake height profiles that indicate the lateral size of the GO flakes (the horizontal distance on top of plateaus) that fall along the red lines on the AFM images. The height profiles of GO flakes also showed that the flakes have a thickness of approximately 1 nm, which is the characteristic thickness of monolayer GO flakes, and verified the formation of single-layer GO aqueous dispersions without any aggregation.

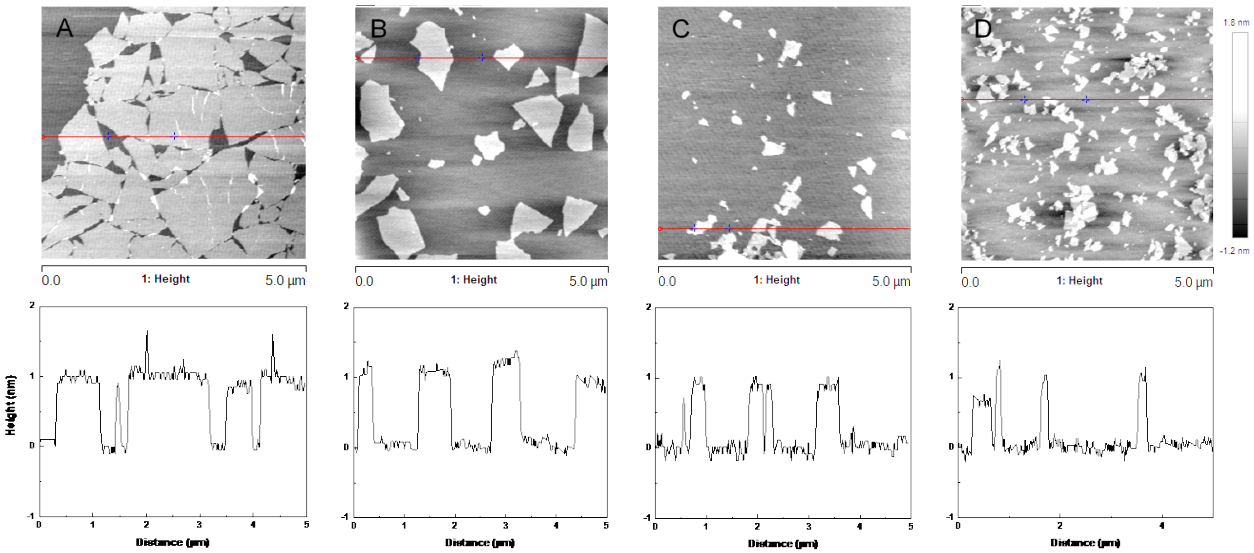

Figure 1: AFM images of GO flakes deposited on mica sheets (top) and height profiles of GO flakes (bottom) along the red lines represented on AFM images at different sonication times (A) 0 h, (B) 0.5 h, (C) 4 h, and (D) 8 h .

The GO flake size distributions obtained at various sonication times are presented in Figure 2. It can be seen that the average area of GO flakes is 1.06 μm^2 (0 h) prior to tip sonication but decreases to 0.14 μm^2, 0.03 μm^2 and 0.01 μm^2 after 0.5 h, 4 h and 8 h of sonication, respectively. Although the GO-0 (representing 0 h of sonication) and GO-0.5 dispersions have a substantial proportion of larger GO flakes, their average size is much smaller than the larger flakes due to the presence of several smaller GO flakes in the dispersion. As a result, the average flake size by itself is insufficient to represent the difference in the GO flake size for various samples. However, it can be depicted from the size distributions that GO-4 and GO-8 dispersions are much less polydispersed than those of GO-0 and GO-0.5 dispersions; thus, confirming that the mean size of GO-4 and GO-8 flakes are maintained at less than 0.03 μm^2 and 0.01 μm^2, respectively. These GO dispersions were used to study the impact of GO size on the morphology and performance of PA TFN membranes.

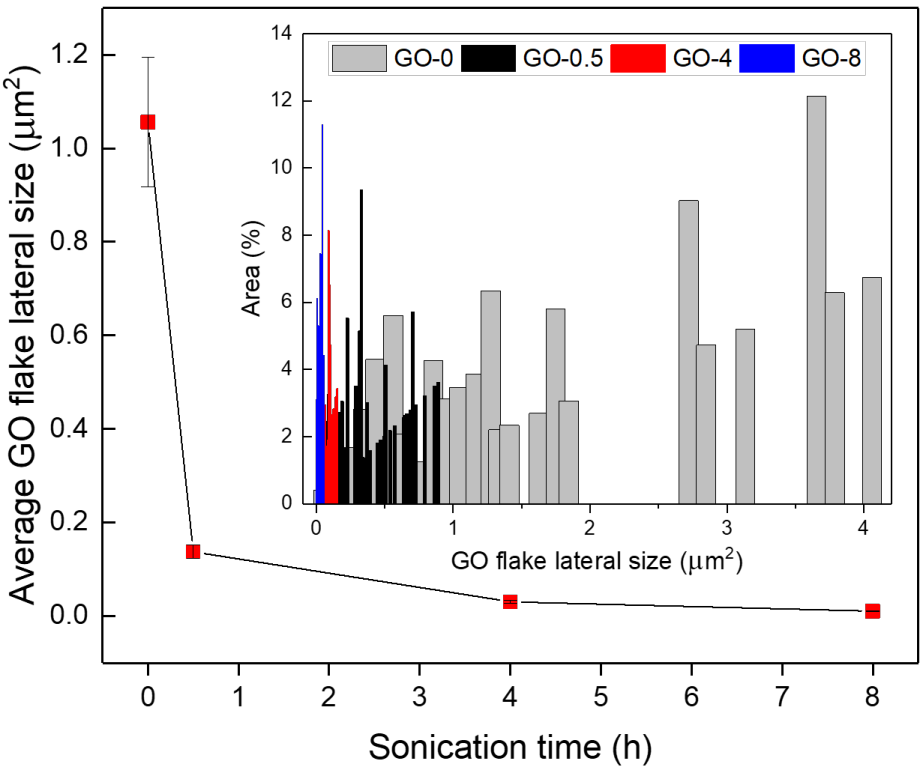

Figure 2: Average GO flake area at various durations of sonication. The size distributions were obtained from AFM images by measuring the area of nearly 200 GO flakes for each sample using the ImageJ software. Inset plot: Histograms depicting the GO flake size distributions at various durations of tip sonication.

3.2 Membrane characterization

The changes in the surface chemistry of the fabricated membranes were observed using FTIR spectra as shown in Figure 3. The characteristic peaks of the PSf were detected at 1503 cm^{-1}, 1411 cm^{-1}, 1237 cm^{-1}, 1293 cm^{-1} and 1148 cm^{-1}, which are ascribed to the C–H symmetric deformation in $C(CH_3)_2$, C=C aromatic ring stretch, C–O–C asymmetric stretch of the aryl-O-aryl group, O=S=O asymmetric stretch and O=S=O symmetric stretch of the PSf, respectively [38, 39]. The peaks at 1542 cm^{-1} (C–N stretching and N-H bending of amide II) and 1661 cm^{-1} (C=O stretching of amide I) validated the PA layer development on the substrate via the IP reaction. The increasing intensity of the 1542 cm^{-1} band for the TFN membranes indicates possible interaction between GO

flakes and PA, resulting in the formation of more amide bonds. The increasing transmission intensity at 1661 cm^{-1} is evident for the TFN membranes and can be attributed to the development of new amide bonds due to the reaction between the GO flakes' carboxyl groups (–COOH) with the amine groups ($–NH_2$) of MPD. The peak at 1713 cm^{-1} corresponds to the carboxyl groups (C=O) of GO, which explains its absence on the TFC membrane spectrum [28]. In addition, the peak intensity at 2854 cm^{-1} and 2925 cm^{-1} (C-H symmetric and asymmetric stretching, respectively) increased upon GO flake incorporation due to the presence of more C–H bonds from GO flakes. Finally, the FTIR spectra of the TFN membranes demonstrated stronger peaks than the TFC membrane at 3333 cm^{-1} because of the hydroxyl group (-OH) stretching of GO flakes. Overall, the above FTIR results validated the successful integration of GO flakes inside the PA layer through covalent bonding during the IP reaction.

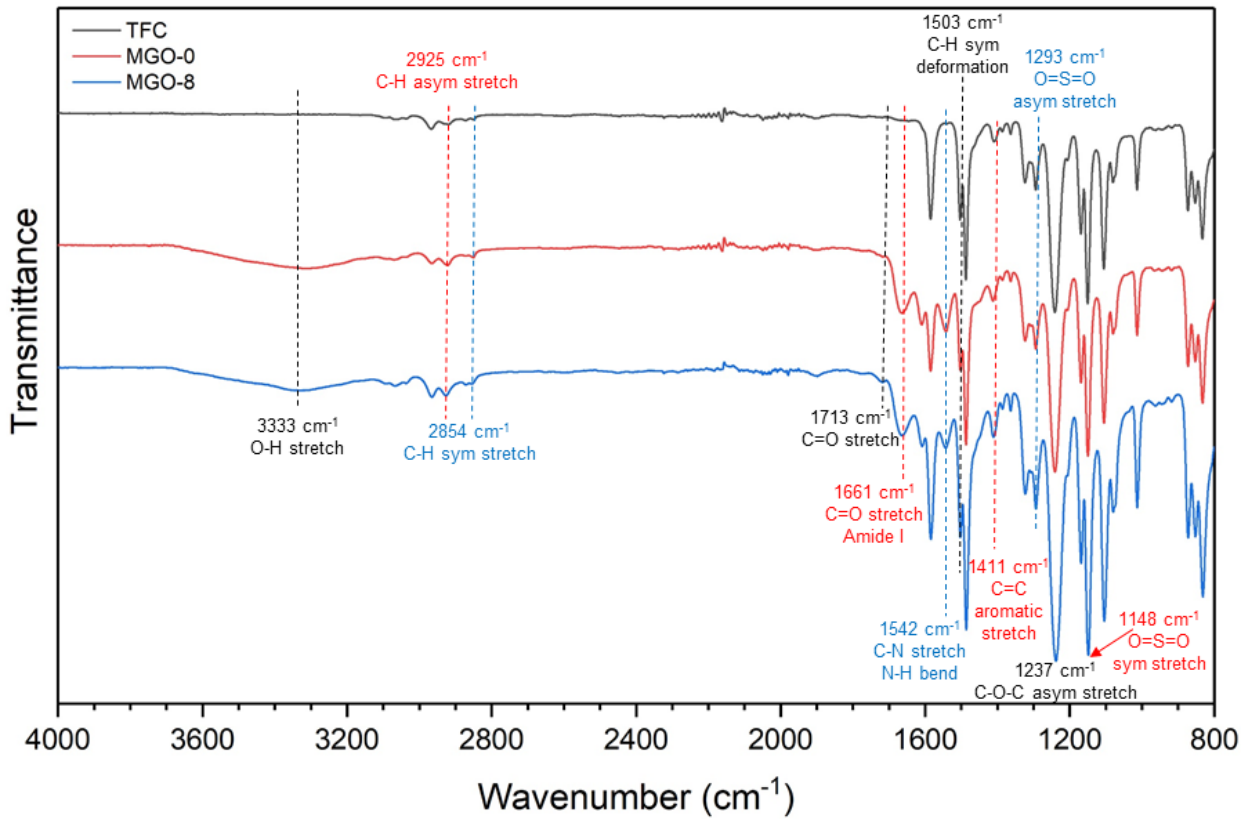

Figure 3: FTIR spectra of TFC and GO-modified TFN membranes.

The SEM images of the PA surface and cross-section morphology of the TFC and GO-modified TFN membrane samples are presented in Figure 4 and Figure 5, respectively. The characteristic ridge-and-valley structures of the PA layer are visible on the surfaces of all the membrane samples. However, the integration of GO flakes in the PA layer significantly altered the membrane surface morphology. It is evident from the top surface SEM (Figure 4) and AFM images (Figure 6) that the GO-modified TFN membranes have much smoother surfaces with smaller PA ridge height than the pristine TFC membrane. The PA layer ridge-and-valley structure develops when MPD diffuses from the aqueous to the organic phase and reacts with TMC. The GO-modified TFN membranes demonstrated smoother PA surface mainly because the horizontally oriented GO flakes on the PSf substrate surface retarded MPD diffusion into the organic phase. The delay in IP reaction can be attributed to the steric-hindrance effect of the GO flakes. Additionally, both TMC and MPD can react with the oxygen functional groups of GO, which can reduce the reaction rate between them.

Unlike the TFC membrane, all the GO-modified TFN membranes can be observed to have some smooth patches with no ridge-and-valley structures, which are encircled in red borders (Figure 4). These smooth patches result from the GO flakes obstructing the reaction between MPD and TMC. Hence, larger patches can be observed on membranes incorporated with larger GO flakes. For instance, MGO-0 exhibited the most defective PA layer with patches in the range of 2-10 µm (Figure 4B) followed by that of MGO-0.5 with smaller patches of 1-2 µm (Figure 4C). A more uniform distribution of patches that is significantly smaller in size than those of MGO-0 and MGO-0.5 can be noticed on the surfaces of MGO-4 and MGO-8 (Figure 4D and E). This is because the number of GO flakes in the GO dispersion increases upon increasing the sonication time. Hence,

306 0.01 wt.% dispersion of GO-8 has more GO flakes than that of GO-0 with much smaller lateral
307 sizes that disperse more uniformly in the PA layer and create minimal defects in the selective layer.
308
309 As apparent from the cross-section images (Figure 5), the PA layer height of the GO-modified
310 membranes are smaller than those of the pristine membrane. It should be noted that the PA layer
311 height here refers to the average height of the PA layer from the PSf substrate to the top of the PA
312 ridge structure, and not the thickness of PA skin. The cross-section SEM images were utilized to
313 determine the average PA layer height for all the membranes, as presented in Figure 5F. It can be
314 observed that the overall height of the PA layer ridges decreases as the size of incorporated GO
315 flakes decreases at higher sonication times. The GO flakes interrupt the growth of PA ridge-and-
316 valley structures during the IP process [40]. Additionally, the better distribution of smaller GO
317 flakes in the PA leads to the development of thinner and more uniform selective layer. Therefore,
318 it can be concluded that GO flakes with smaller lateral size are more desirable for less defective
319 PA layer.
320

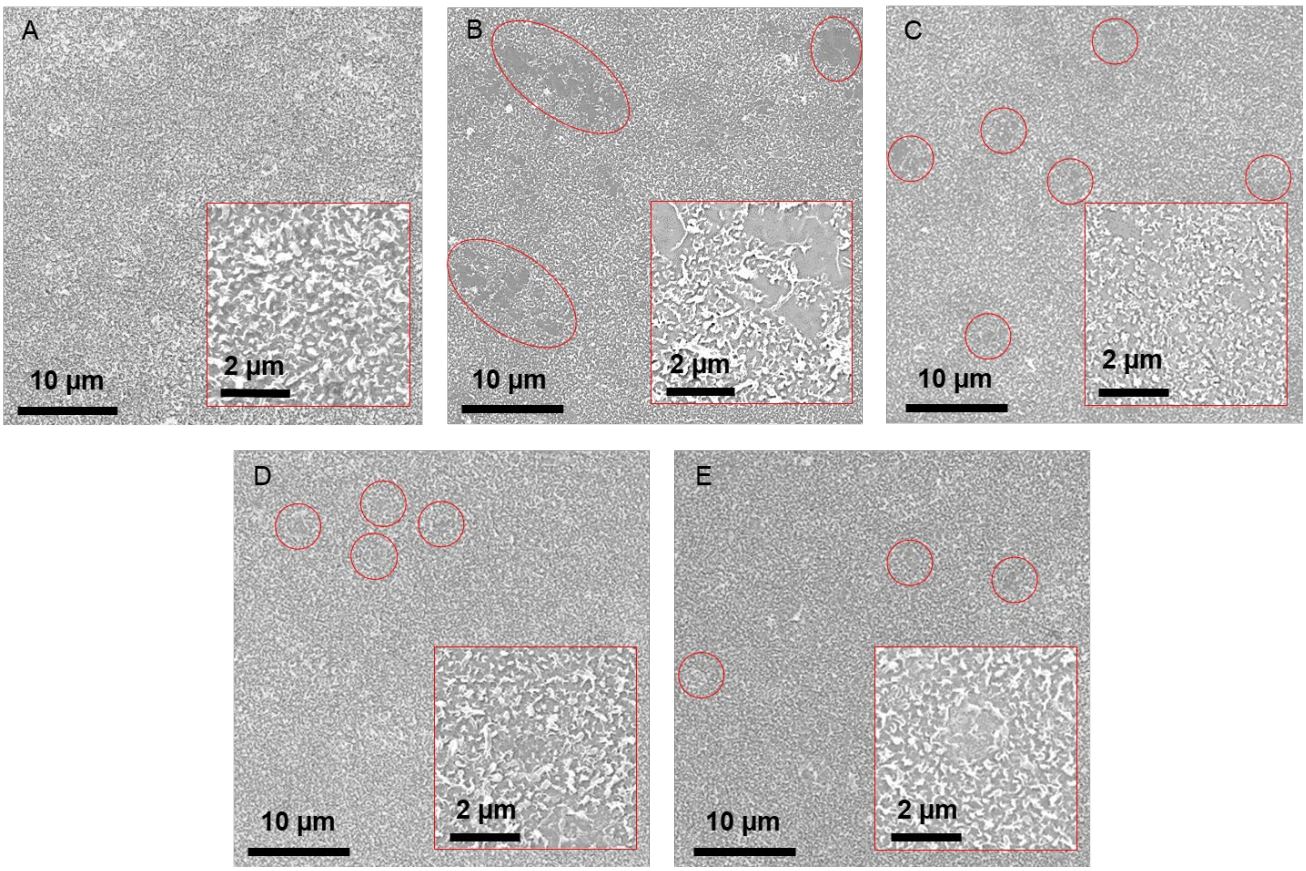

321

322 Figure 4: SEM images of PA surface: (A) TFC, (B) MGO-0, (C) MGO-0.5 (D) MGO-4, and (E) MGO-8
323 membranes. The GO loading was fixed at 0.01 wt./v% for all the TFN membranes. The red borders present
324 the smooth patches that form when GO flakes impede the IP reaction.

325

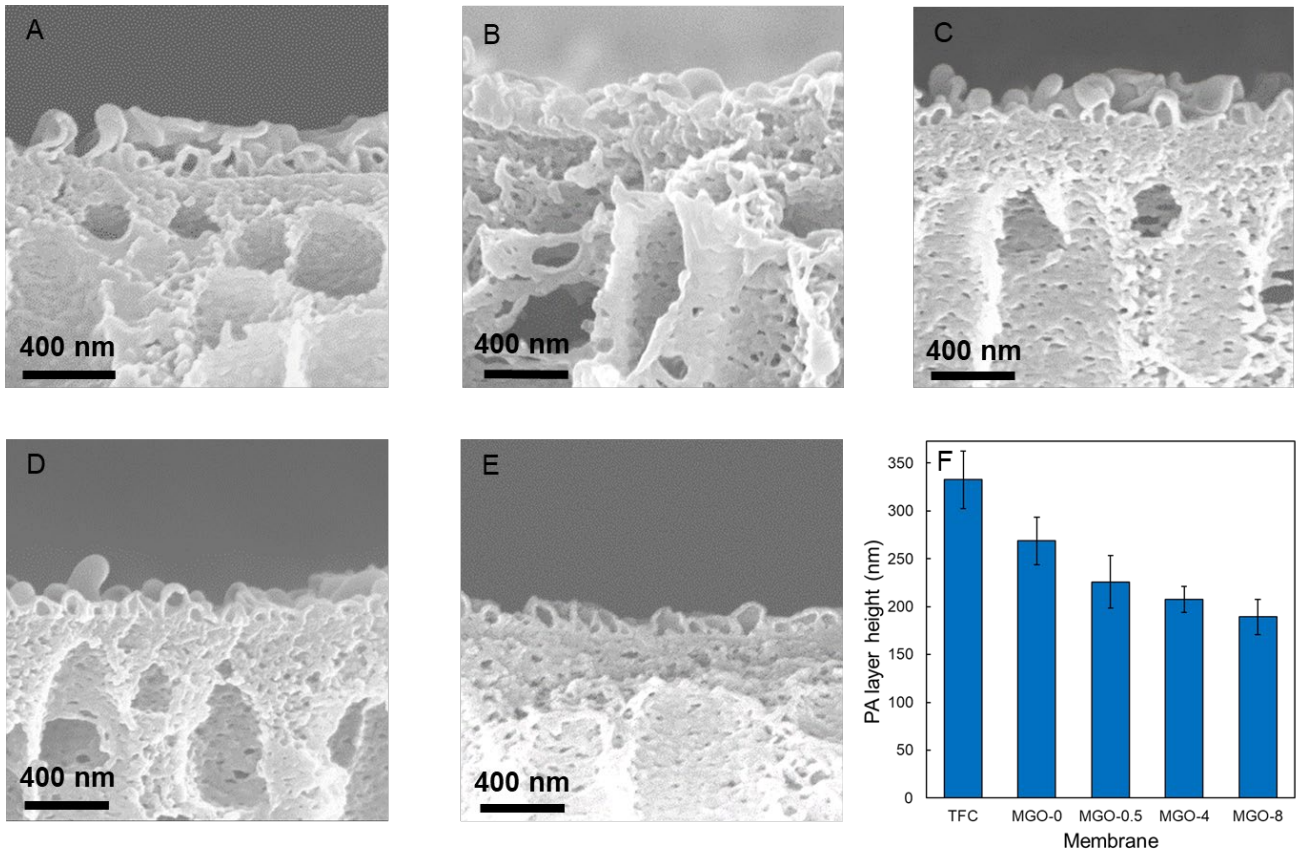

Figure 5: SEM images of membrane cross-section, (A) TFC, (B) MGO-0, (C) MGO-0.5 (D) MGO-4, and (E) MGO-8 membranes. (F) PA layer height of the TFC and GO-modified TFN membranes. The GO loading was fixed at 0.01 wt./v% for all the TFN membranes.

The GO flake size effect on the PA layer surface roughness was analyzed from the surface topography obtained with AFM. Figure 6A-E presents the 3-D AFM images of the fabricated membranes. The maximum (R_{max}), mean (R_a) and root mean square (R_q) membrane roughness are shown in Figure 6F. The pristine TFC membrane surface was the roughest with a R_a value of 61.0 nm. The GO-modified TFN membranes demonstrated much smoother surfaces than the TFC membrane due to GO flakes slowing down the IP reaction. Since the development of the PA layer's "ridge-and-valley" structures depends on the reaction between TMC and MPD, the retardation of MPD diffusion by GO flakes restricted the formation of the PA protrusions during the IP reaction.

The MGO-0 membrane demonstrated the smoothest surface (R_a = 36.0 nm) because the GO-0 flakes with the largest lateral size (< 5 μm) inhibited MPD diffusion most effectively; thus, resulting in the formation of lesser and smaller PA protrusions (Figure 6B). The roughness of GO-modified TFN membranes was observed to increase with a decrease in GO flake size (Figure 6F) due to the better dispersion and reduced aggregation of smaller GO flakes. Hence, the reduced flake area of the smaller GO flakes could not impede the MPD diffusion as efficiently as the large GO flakes, which resulted in rougher PA layer formation. A higher surface roughness corresponds to a larger specific membrane surface area, which can promote water transport across the membrane.

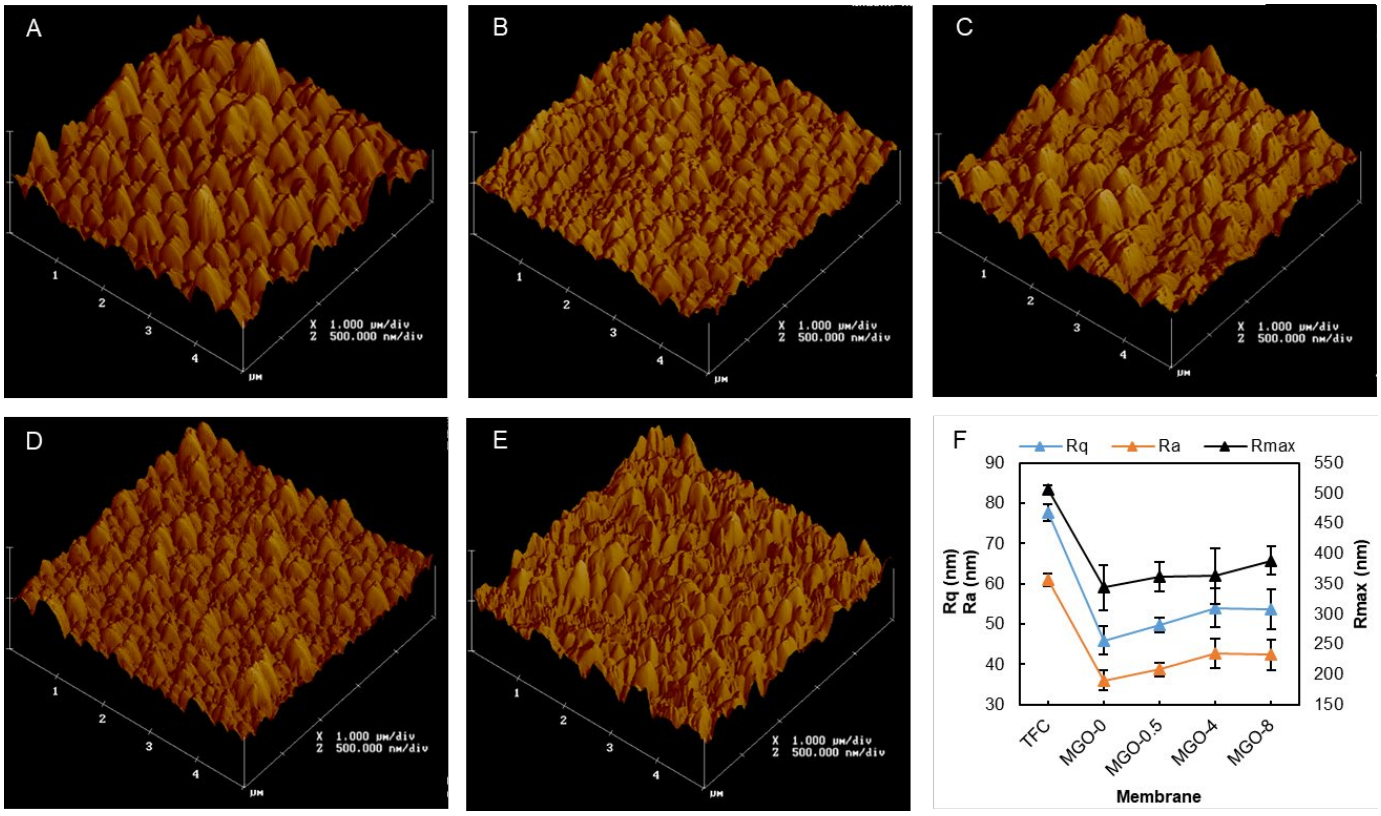

Figure 6: AFM images representing PA surface topography of (A) TFC, (B) MGO-0, (C) MGO-0.5 (D) MGO-4, and (E) MGO-8 membranes. (F) Surface roughness parameters of the developed membranes obtained by examining three arbitrarily chosen membrane areas (5 μm × 5 μm).

353 To further assess membrane surface properties, the wettability of all the membrane samples was
354 decided from the water contact angle measurements. Membrane surface wettability is a crucial
355 factor as it can strongly influence the membrane performance. Overall, the GO TFN membranes
356 demonstrated much lower contact angles than the TFC membrane (82.8°) owing to the existence
357 of hydrophilic oxygen-containing functional groups on GO flakes that significantly improved
358 membrane wettability (Figure 7A). The enhanced hydrophilicity of the GO-modified membranes
359 is likely to promote water absorption and contribute to improved water flux across the TFN
360 membranes. As evident from Figure 7A, the contact angle of the GO-modified membranes
361 decreased slightly from 66.3° (MGO-0) to 53.7° (MGO-8) with decreasing GO flake size. The
362 increased hydrophilicity of the GO-modified membranes with smaller GO flakes can be attributed
363 to the uniform GO flake dispersion in the PA layer. Moreover, the diminished thickness (Figure 5)
364 and increased roughness (Figure 6) of the PA layer with smaller GO flakes facilitated the easy
365 permeation of water droplets through the PA layer.
366
367 The zeta potential of the fabricated membranes obtained as a function of the pH ranging from 3 to
368 10 is presented in Figure 7B. It can be noticed that all the membranes were negatively-charged at
369 pH greater than 5.9 because of the carboxyl group dissociation and amine group deprotonation in
370 the PA structure [41]. The positive charge of the membranes at lower pH could be ascribed to the
371 amine group protonation. It has been previously reported that integration of GO inside the PA
372 causes the TFN membrane surface to be more negatively charged than the TFC membrane owing
373 to the existence of the plentiful oxygen-containing functional groups, like the carboxyl groups, on
374 GO flakes that deprotonate at alkaline conditions to provide more negative charges. As a result,
375 the TFC membrane has the least negatively-charged, and MGO-4 and MGO-8 have the most

negatively-charged PA surfaces across the considered pH range. The isoelectric point (IEP) at which the PA layer is electrically neutral is shown in Figure 7B. The IEPs of the membranes shift to lower pH values upon the addition of GO flakes in the PA layer because of the existence of the acidic functional groups on GO flakes [42]. Additionally, the negative charge of all the membranes increases as the pH increases due to charge accumulation resulting from the adsorption of negatively-charged chloride ions on the membrane surface. Overall, the reduced zeta potentials of the GO-modified membranes established the successful integration of the GO flakes into the PA layer.

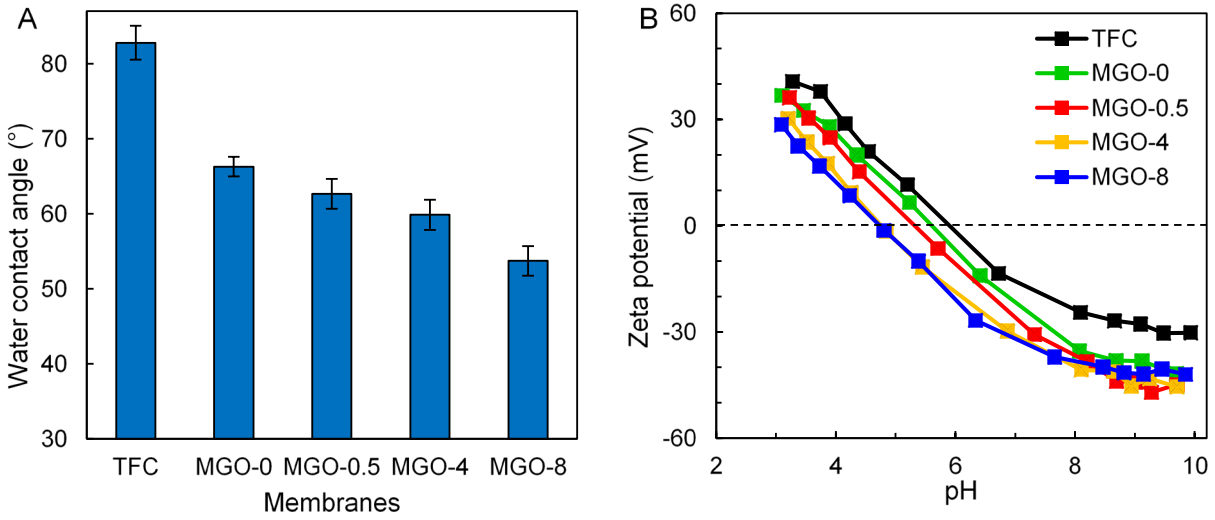

Figure 7: (A) Initial water contact angles and (B) surface charge measurements as a function of pH for fabricated TFC and GO-modified TFN membranes.

3.3 Membrane performance evaluation

The performance results of pristine TFC and GO-modified TFN FO membranes in both membrane orientations with DI water FS and 0.5 M NaCl DS are shown in Figure 8. The water flux across

all the GO-modified TFN membranes was greater than the pristine membrane as a result of their improved hydrophilicity and thinner PA active layer. Additionally, the water flux increased with a decrease in GO flake size (Figure 8A) due to the increased roughness and reduced thickness of the PA layer that increased the membrane surface area and reduced the water transport resistance across the PA layer [36]. The low water flux of MGO-0 can be associated with its defective PA layer that failed to form a highly selective solute barrier; thus, reducing the effective osmotic driving force. The larger flakes of GO-0 likely resulted in more impervious area; thereby, reducing the effective PA area on the MGO-0 surface. MGO-8 exhibited the highest water flux of 24.7 $Lm^{-2}h^{-1}$ (41.9 $Lm^{-2}h^{-1}$) in the AL-FS (AL-DS) orientations that corresponded to a flux enhancement of 89.6% (62.4%) than that of the pristine TFC membrane. Besides, the improvement in water flux with smaller GO flakes could be ascribed to the reduced tortuosity in the PA layer created by shorter water channels developed at the GO-PA interface [43].

The water flux obtained in the AL-DS arrangement was considerably higher compared to the AL-FS membrane orientation owing to the absence of ICP when DI water was used as FS on the support layer side of the membrane. As indicated in several earlier studies, dilutive ICP significantly lowers the effective osmotic driving force at the membrane support layer and active layer interface in AL-FS orientation [8]. The significant difference of water fluxes between AL-DS and AL-FS modes is also an indication of the high degree of ICP effect in the synthesized membranes. This implies the potential of further improving the water flux performances of these membranes by optimizing the support layer structure.

Figure 8B exhibits the SRSF of the developed membranes. A smaller SRSF value indicates greater membrane selectivity, which is preferable for FO membranes. The SRSF of the MGO-0 membrane in both orientations was considerably higher than that of the TFC membrane because the largest GO flake size (GO-0) formed a defective non-uniform PA layer with large non-selective patches that likely enhanced the salt flux. As a result, MGO-0 demonstrated the highest SRSF value of 0.54 g/L in AL-FS mode compared to other membranes. The SRSF of MGO-0.5 was comparable to that of the TFC membrane; however, the SRSF values of the TFN membranes reduced with a decrease in GO flake size. The membrane selectivity improved with smaller GO flakes (GO-4 and GO-8) because they dispersed more uniformly in the PA layer and significantly reduced the PA defects compared to the GO-0 flakes.

The higher SRSF values for membranes with larger GO flakes indicate that the defective PA layer with looser dynamic pore structure allowed relatively more draw solute to diffuse to the FS. Therefore, GO flakes with smaller lateral size are highly desirable for developing non-defective PA TFN membranes. The MGO-8 can be considered as the best performing membrane among the other GO-modified TFN membranes based on the FO performance as it exhibited a substantial enhancement in water flux without deteriorating the membrane selectivity. MGO-8 demonstrated a 51% increment in water flux and a 61% decline in SRSF compared to the MGO-0 membrane, suggesting that the GO lateral size plays a vital role in the membrane performance.

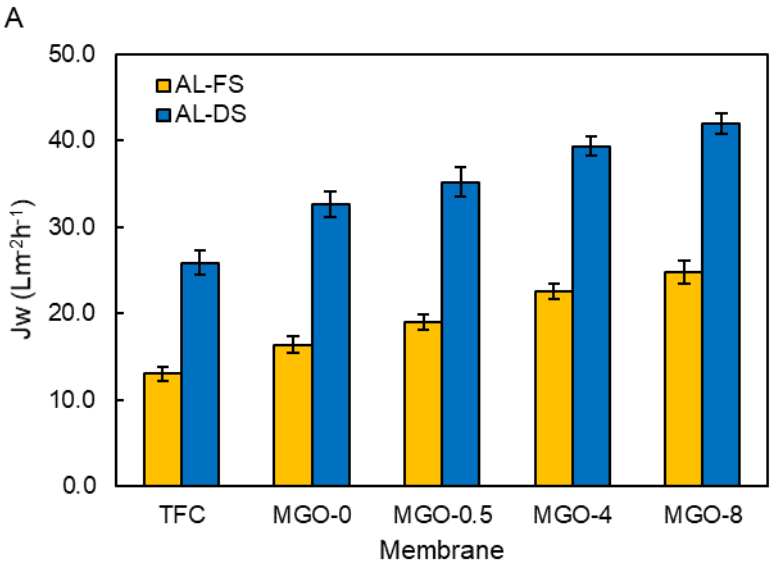

434

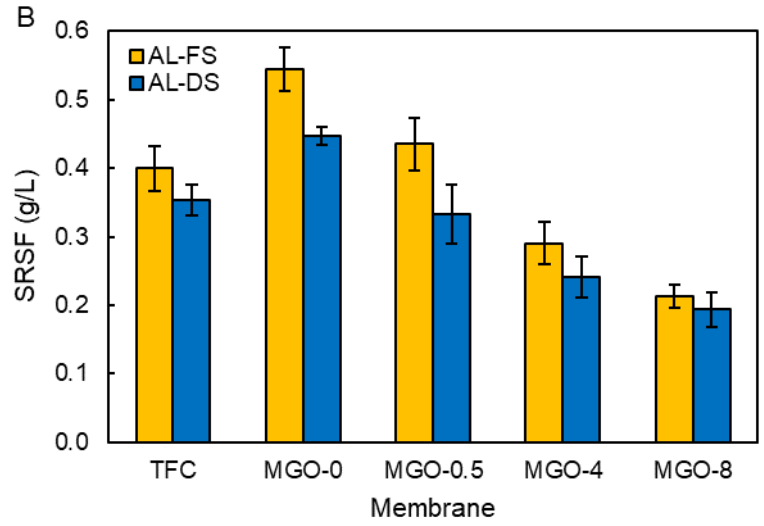

435

436 Figure 8: FO performance of the developed TFC and GO-modified TFN membranes in AL-FS/AL-DS
437 arrangements: (A) water flux and (B) SRSF.

438 ***3.4 Membrane transport parameters***

439 Table 1 lists the separation parameters of the membranes developed in this study. Both A and B
440 parameters of the GO-modified TFN membranes were found to be higher than those of the pristine
441 TFC membrane. TFN membrane with smaller GO flake lateral size showed higher A values and
442 lower B values comparatively. For instance, the MGO-8 membrane with the smallest GO flake

size demonstrated a 52% increase in the A value and a 33% decrease in the B value compared to the MGO-0 membrane with the largest GO flake size. A more uniform, hydrophilic and thinner PA layer formation with fewer defects and better GO dispersion resulted in the improved selectivity and permeability of membranes incorporated with GO of smaller flake size. The membrane separation parameters are in good agreement with the performance results presented in Figure 8.

The intrinsic selectivity ratio (B/A) presented in Table 1 is an essential factor for determining the selectivity of FO membranes. A higher membrane selectivity is denoted by a smaller B/A ratio. The MGO-0 exhibited the highest B/A value of 0.55 bar; whereas, MGO-8 demonstrated the best selectivity with the smallest B/A value of 0.24 bar. The B/A values of the membranes agree well with the previously discussed SRSF values (Figure 8B).

Table 1: Separation parameters of the fabricated membranes determined using the algorithm established by Tiraferri et al. [37].

Membrane	A ($Lm^{-2}h^{-1}bar^{-1}$)	B ($Lm^{-2}h^{-1}$)	B/A (bar)
TFC	1.29	0.51	0.40
MGO-0	2.44	1.33	0.55
MGO-0.5	2.65	1.05	0.40
MGO-4	3.04	0.85	0.28
MGO-8	3.71	0.89	0.24

3.5 Membrane fouling study

The fouling propensity of the TFC and GO-modified TFN membranes during FO operation was examined via crossflow fouling tests in AL-FS membrane orientation while taking the DS dilution into consideration. MGO-0 and MGO-8 incorporated with the largest and smallest GO flakes, respectively, were chosen to evaluate the effect of GO flake size on the fouling propensity of the TFN membranes. The normalized water flux (Jw/Jw, 0) of the membranes during the fouling test, with synthetic wastewater as FS and initial water flux (Jw,0) adjusted to ~ 25 $Lm^{-2}h^{-1}$, is presented in Figure 9. A reduction in normalized water flux was observed for all membranes as soon as sodium alginate and silica were introduced into the FS due to foulant buildup on the membrane surfaces. The TFC membrane demonstrated a continuous and much rapid flux decline compared to the GO-modified membranes and reached a normalized flux of 0.77 for an accumulated permeate volume of 100 mL during the fouling test. The TFC membrane demonstrated the highest flux decline due to its rougher and less hydrophilic PA surface, which facilitated better adhesion of sodium alginate and silica to the membrane surface. The deposited foulant layer considerably reduced the flux by increasing transport resistance and decreasing permeability across the membrane.

Conversely, the GO-modified membranes exhibited better antifouling property and MGO-8 showed the lowest flux decline. The normalized flux of MGO-8 and MGO-0 membranes eventually stabilized at 0.94 and 0.88, respectively. As discussed in the previous sections, the increased smoothness, hydrophilicity and surface negativity of the TFN membranes, especially MGO-8, enhanced their fouling resistance and selectivity more than the pristine membrane by restraining hydrophobic foulant attachment on their surfaces and repelling negatively charged salt ions.

The GO TFN membranes created a thin film of water molecules on their hydrophilic surfaces through hydrogen bonding that minimized the adsorption of hydrophobic sodium alginate and silica cake layer on the membrane surfaces [44]. The smooth PA surfaces of GO TFN membranes also minimized the accumulation of foulants by providing them fewer adhesion sites. Finally, the negatively charged hydroxyl, epoxide and carboxyl functional groups on the GO flakes facilitated repulsion of the negatively charged foulants from the TFN membranes surfaces; thus, improving their antifouling property [27].

Moreover, it was observed that the fouling propensity of MGO-0 was higher than that of MGO-8. The higher flux decline with MGO-0 can be associated with its higher SRSF value compared to that of MGO-8. Although MGO-0 demonstrated a smoother surface than the MGO-8 membrane, its poor selectivity accelerated fouling on its surface because of the occurrence of electrostatic attraction between the charged foulants and the DS ions [45]. Additionally, MGO-8 demonstrated a higher negative surface charge than the MGO-0 (Figure 7B), which minimized the buildup of negatively charged sodium alginate molecules on its surface.

Following the fouling tests, the membranes were physically cleaned, and their flux recovery was obtained to determine the reversibility of the sodium alginate and silica fouling. The normalized membrane water flux before and after hydraulic cleaning is presented in Figure 10. The normalized flux for all membranes increased after the cleaning process, which indicates that the fouling is reversible to a certain extent. The GO-modified TFN membranes (MGO-0 and MGO-8) achieved a high flux recovery of around 98%; whereas, the TFC membrane attained a relatively lower flux

recovery of 80% after an hour of hydraulic rinsing at 12.6 cm/s. The much smoother surfaces of TFN membranes facilitated easier removal of foulants due to the presence of fewer adhesive sites on the PA layer. Additionally, the increased surface negative charge and hydrophilicity of the TFN membranes decreased the foulant- membrane interaction leading to the formation of a loose foulant cake layer, which could be easily detached with the shear force from the high cross-flow velocity during the cleaning process. Therefore, it can be confirmed that the TFC membrane's fouling was partially reversible, while that of GO-modified TFN membranes was almost entirely reversible by physical cleaning. The above results suggest that TFN membranes incorporated with smaller GO flakes (MGO-8) possess better antifouling properties.

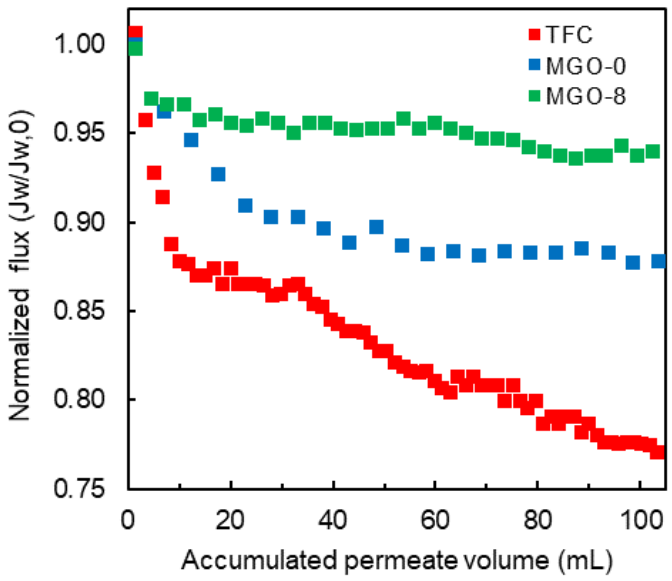

Figure 9: Normalized flux of the TFC, MGO-0 and MGO-8 membranes throughout the FO fouling test. The normalized flux was attained by dividing the water flux obtained after every 5 minutes interval by the initial water flux (~25 $Lm^{-2}h^{-1}$). NaCl (0.75 M to 2 M) and synthetic wastewater (200 mg/L of sodium alginate and colloidal silica) were used as DS and FS, respectively.

519

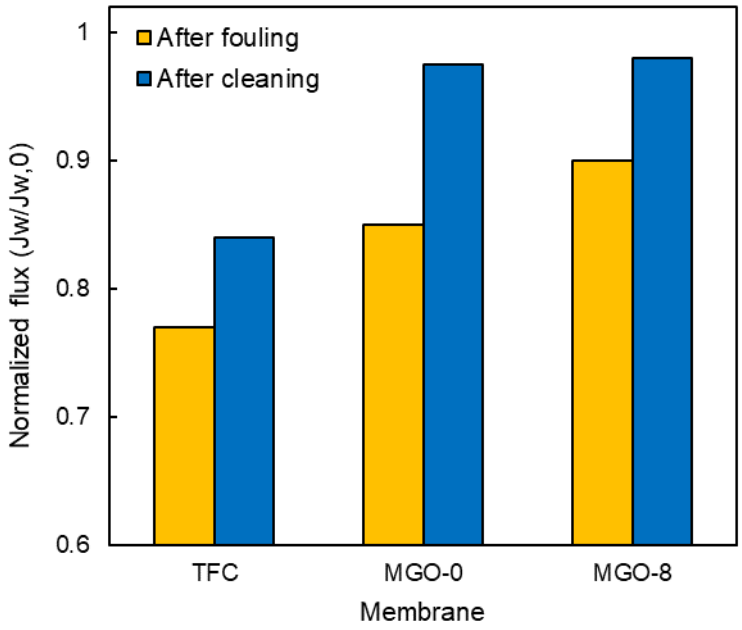

520

521 Figure 10: Normalized flux of the TFC, MGO-0 and MGO-8 membranes before and after hydraulic
522 cleaning (Hydraulic cleaning conditions: FS and DS, DI water; membrane orientation, AL-FS; cross-flow
523 velocity, 12.6 cm/s; physical rinsing duration, 1 h; temperature, 22 °C).

524

525 **4. Benchmarking membrane performance**

526 Table 2 shows the performance of GO-incorporated TFN FO membranes developed in this study
527 and those reported in the literature. An efficient FO membrane should demonstrate both high
528 selectivity and permeability. The TFN membranes fabricated in this study exhibited a similar or
529 better performance than those reported in the literature but at a much lower GO loading and DS
530 concentration. The MGO-8 membrane incorporated with the smallest GO flakes exhibited higher
531 water flux than other recently developed GO TFN FO membranes while maintaining membrane
532 selectivity. Thus, the reduction of GO flake size can be a possible strategy for fabricating highly-
533 efficient FO membranes.

534

535 Table 2: FO performance summary of the various GO-modified PA TFN flat sheet in AL-FS orientation.

Membrane	Filler	DS/ FS	J_w ($Lm^{-2}h^{-1}$)	SRSF (g/L)	Reference
TFC	N/A	0.5 M NaCl/ DI water	13.04	0.40	This work
MGO-0	0.01 wt.% GO (1.06 μm^2)	0.5 M NaCl/ DI water	16.38	0.54	This work
MGO-8	0.01 wt.% GO (0.01 μm^2)	0.5 M NaCl/ DI water	24.72	0.21	This work
TFC-400	0.04 wt.% GO	0.5 M NaCl/ DI water	17.5	0.11	[27]
TFN 0.1	0.1 wt.% GO	1.0 M NaCl/ DI water	14.5	0.18	[46]
TFC–PDA/GO-0.5	5 mL of 0.05 wt.% GO dispersion	1.0 M NaCl/ DI water	24.3	0.16	[47]
PA-GO2	2 mL of 0.05 wt.% GO dispersion	0.3 M Na_2SO_4/ DI water	10.5	1.78	[48]
GO-FO-5	0.0175 wt.% PVP modified GO	2 M NaCl/ 10 mM NaCl	14.6	1.0	[28]

536

537 **5. Conclusions**

538 This study explored the effect of GO flake lateral size on the TFN FO membrane performance.
539 Different GO flake sizes were prepared by subjecting GO to different duration of sonication. GO
540 was incorporated inside the PA layer during the IP process by dispersing 0.01 wt.% of GO flakes
541 in the amine solution. Generally, the GO-modified TFN membranes demonstrated better FO
542 performance and antifouling property than the unmodified TFC membrane due to their thinner PA
543 layer, improved membrane surface hydrophilicity, smoother and negatively charged surfaces. The
544 largest GO flakes (GO-0, without tip sonication) were found to create a more defective PA layer
545 by hindering the MPD diffusion into the organic phase and resulting in the formation of a low
546 selective membrane (MGO-0) with a SRSF of 0.54 g/L. However, the TFN membrane
547 performance enhanced on incorporating smaller GO flakes due to a more uniform GO dispersion

548 that reduced PA layer defects. The TFN membrane incorporated with the smallest GO flakes
549 (MGO-8, tip sonicated for 8 h) showed a 51% higher water flux and 61% lower SRSF than the
550 MGO-0 membrane when tested with 0.5 M NaCl DS and DI water FS in AL-FS orientation. MGO-
551 8 also demonstrated better anti-fouling property than MGO-0 due to its augmented surface
552 negativity, improved hydrophilicity and selectivity. These results confirm that the TFN membrane
553 performance can be considerably influenced by GO flake lateral size and that smaller GO flakes
554 can minimize PA defects; thus, improving membrane flux and selectivity. This study provides a
555 guideline for future studies and highlights the significance of an accurate evaluation of the impact
556 of nanomaterial physical properties on membrane performance rather than attributing the
557 improvement in membrane performance solely to chemical modification of nanomaterials.
558

Acknowledgment

The research reported in this paper was supported by King Abdullah University of Science and Technology (KAUST), Saudi Arabia through the Competitive Research Grant Program – CRG2017 (CRG6), Grant # URF/1/3404-01. H.K.S. and Y.C. acknowledge the support provided by the Australian Research Council under the Future Fellowships scheme (FT140101208 & FT160100107), ARC Industry Hub (IH170100009), Discovery Project (DP180102210) and Bhutan Trust Fund for Environmental Conservation (Grant No. MB0167Y16).

References

[1] K.L. Lee, R.W. Baker, H.K. Lonsdale, Membranes for power generation by pressure-retarded osmosis, Journal of Membrane Science, 8 (1981) 141-171.

[2] R. Thiruvenkatachari, M. Francis, M. Cunnington, S. Su, Application of integrated forward and reverse osmosis for coal mine wastewater desalination, Separation and Purification Technology, 163 (2016) 181-188.

[3] E. Yang, C.-M. Kim, J.-h. Song, H. Ki, M.-H. Ham, I.S. Kim, Enhanced desalination performance of forward osmosis membranes based on reduced graphene oxide laminates coated with hydrophilic polydopamine, Carbon, 117 (2017) 293-300.

[4] S. Xu, F. Li, B. Su, M.Z. Hu, X. Gao, C. Gao, Novel graphene quantum dots (GQDs)-incorporated thin film composite (TFC) membranes for forward osmosis (FO) desalination, Desalination, (2018).

[5] J. Zhang, Q. She, V.W.C. Chang, C.Y. Tang, R.D. Webster, Mining Nutrients (N, K, P) from Urban Source-Separated Urine by Forward Osmosis Dewatering, Environmental Science & Technology, 48 (2014) 3386-3394.

[6] K. Lutchmiah, A.R.D. Verliefde, K. Roest, L.C. Rietveld, E.R. Cornelissen, Forward osmosis for application in wastewater treatment: A review, Water Research, 58 (2014) 179-197.

[7] T.Y. Cath, N.T. Hancock, C.D. Lundin, C. Hoppe-Jones, J.E. Drewes, A multi-barrier osmotic dilution process for simultaneous desalination and purification of impaired water, Journal of Membrane Science, 362 (2010) 417-426.

[8] N. Akther, S. Daer, S.W. Hasan, Effect of flow rate, draw solution concentration and temperature on the performance of TFC FO membrane, and the potential use of RO reject brine as a draw solution in FO–RO hybrid systems, Desalination and Water Treatment, 136 (2018) 65-71.

[9] V.H. Tran, S. Lim, D.S. Han, N. Pathak, N. Akther, S. Phuntsho, H. Park, H.K. Shon, Efficient fouling control using outer-selective hollow fiber thin-film composite membranes for osmotic membrane bioreactor applications, Bioresource Technology, 282 (2019) 9-17.

[10] R.E. Wrolstad, M.R. Mcdaniel, R.W. Durst, N. Micheals, K.A. Lampi, E.G. Beaudry, Composition and sensory characterization of red raspberry juice concentrated by direct-osmosis or evaporation, Journal of Food Science, 58 (1993) 633-637.

[11] C. Aydiner, S. Topcu, C. Tortop, F. Kuvvet, D. Ekinci, N. Dizge, B. Keskinler, A novel implementation of water recovery from whey: “Forward–reverse osmosis” integrated membrane system, Desalination and Water Treatment, 51 (2013) 786-799.

[12] N. Akther, S. Daer, Q. Wei, I. Janajreh, S.W. Hasan, Synthesis of polybenzimidazole (PBI) forward osmosis (FO) membrane and computational fluid dynamics (CFD) modeling of concentration gradient across membrane surface, Desalination, 452 (2019) 17-28.

[13] N. Akther, A. Sodiq, A. Giwa, S. Daer, H.A. Arafat, S.W. Hasan, Recent advancements in forward osmosis desalination: A review, Chemical Engineering Journal, 281 (2015) 502-522.

[14] N. Akther, S. Phuntsho, Y. Chen, N. Ghaffour, H.K. Shon, Recent advances in nanomaterial-modified polyamide thin-film composite membranes for forward osmosis processes, Journal of Membrane Science, 584 (2019) 20-45.

[15] N.Y. Yip, A. Tiraferri, W.A. Phillip, J.D. Schiffman, M. Elimelech, High performance thin-film composite forward osmosis membrane, Environmental Science & Technology, 44 (2010) 3812–3818.

[16] Y.H. Teow, A.W. Mohammad, New generation nanomaterials for water desalination: A review, Desalination, 451 (2019) 2-17.

[17] H.M. Hegab, A. ElMekawy, T.G. Barclay, A. Michelmore, L. Zou, C.P. Saint, M. Ginic-Markovic, Effective in-situ chemical surface modification of forward osmosis membranes with polydopamine-induced graphene oxide for biofouling mitigation, Desalination, 385 (2016) 126-137.
[18] A. Soroush, W. Ma, Y. Silvino, M.S. Rahaman, Surface modification of thin film composite forward osmosis membrane by silver-decorated graphene-oxide nanosheets, Environmental Science: Nano, 2 (2015) 395-405.
[19] D. Ma, S.B. Peh, G. Han, S.B. Chen, Thin-film nanocomposite (TFN) membranes incorporated with super-hydrophilic metal–organic framework (MOF) UiO-66: Toward enhancement of water flux and salt rejection, ACS Applied Materials & Interfaces, 9 (2017) 7523-7534.
[20] X. Song, L. Wang, C.Y. Tang, Z. Wang, C. Gao, Fabrication of carbon nanotubes incorporated double-skinned thin film nanocomposite membranes for enhanced separation performance and antifouling capability in forward osmosis process, Desalination, 369 (2015) 1-9.
[21] D.R. Dreyer, S. Park, C.W. Bielawski, R.S. Ruoff, The chemistry of graphene oxide, Chemical Society Reviews, 39 (2010) 228-240.
[22] H.M. Hegab, A. ElMekawy, L. Zou, D. Mulcahy, C.P. Saint, M. Ginic-Markovic, The controversial antibacterial activity of graphene-based materials, Carbon, 105 (2016) 362-376.
[23] K. Goh, H.E. Karahan, L. Wei, T.-H. Bae, A.G. Fane, R. Wang, Y. Chen, Carbon nanomaterials for advancing separation membranes: A strategic perspective, Carbon, 109 (2016) 694-710.
[24] J. Pang, Z. Kang, R. Wang, B. Xu, X. Nie, L. Fan, F. Zhang, X. Du, S. Feng, D. Sun, Exploring the sandwich antibacterial membranes based on UiO-66/graphene oxide for forward osmosis performance, Carbon, 144 (2019) 321-332.
[25] E. Yang, A.B. Alayande, C.-M. Kim, J.-h. Song, I.S. Kim, Laminar reduced graphene oxide membrane modified with silver nanoparticle-polydopamine for water/ion separation and biofouling resistance enhancement, Desalination, 426 (2018) 21-31.
[26] Y. Yuan, X. Gao, Y. Wei, X. Wang, J. Wang, Y. Zhang, C. Gao, Enhanced desalination performance of carboxyl functionalized graphene oxide nanofiltration membranes, Desalination, 405 (2017) 29-39.
[27] L. Shen, S. Xiong, Y. Wang, Graphene oxide incorporated thin-film composite membranes for forward osmosis applications, Chemical Engineering Science, 143 (2016) 194-205.
[28] X. Wu, R.W. Field, J.J. Wu, K. Zhang, Polyvinylpyrrolidone modified graphene oxide as a modifier for thin film composite forward osmosis membranes, Journal of Membrane Science, 540 (2017) 251-260.
[29] H.M. Hegab, A. ElMekawy, T.G. Barclay, A. Michelmore, L. Zou, C.P. Saint, M. Ginic-Markovic, Fine-tuning the surface of forward osmosis membranes via grafting graphene oxide: Performance patterns and biofouling propensity, ACS Applied Materials & Interfaces, 7 (2015) 18004-18016.
[30] J. Ma, D. Ping, X. Dong, Recent Developments of Graphene Oxide-Based Membranes: A Review, Membranes, 7 (2017) 52.
[31] Y. Qian, X. Zhang, C. Liu, C. Zhou, A. Huang, Tuning interlayer spacing of graphene oxide membranes with enhanced desalination performance, Desalination, 460 (2019) 56-63.
[32] Y. Kang, M. Obaid, J. Jang, I.S. Kim, Sulfonated graphene oxide incorporated thin film nanocomposite nanofiltration membrane to enhance permeation and antifouling properties, Desalination, 470 (2019) 114125.
[33] S. Liu, M. Hu, T.H. Zeng, R. Wu, R. Jiang, J. Wei, L. Wang, J. Kong, Y. Chen, Lateral dimension-dependent antibacterial activity of graphene oxide sheets, Langmuir, 28 (2012) 12364-12372.
[34] X. Sun, Z. Liu, K. Welsher, J.T. Robinson, A. Goodwin, S. Zaric, H. Dai, Nano-graphene oxide for cellular imaging and drug delivery, Nano Research, 1 (2008) 203-212.
[35] A. Tayyebi, O. Akhavan, B.-K. Lee, M. Outokesh, Supercritical water in top-down formation of tunable-sized graphene quantum dots applicable in effective photothermal treatments of tissues, Carbon, 130 (2018) 267-272.

[36] N. Akther, S. Lim, V.H. Tran, S. Phuntsho, Y. Yang, T.-H. Bae, N. Ghaffour, H.K. Shon, The effect of Schiff base network on the separation performance of thin film nanocomposite forward osmosis membranes, Separation and Purification Technology, 217 (2019) 284-293.
[37] A. Tiraferri, N.Y. Yip, A.P. Straub, S. Romero-Vargas Castrillon, M. Elimelech, A method for the simultaneous determination of transport and structural parameters of forward osmosis membranes, Journal of Membrane Science, 444 (2013) 523-538.
[38] G.S. Lai, W.J. Lau, P.S. Goh, A.F. Ismail, Y.H. Tan, C.Y. Chong, R. Krause-Rehberg, S. Awad, Tailor-made thin film nanocomposite membrane incorporated with graphene oxide using novel interfacial polymerization technique for enhanced water separation, Chemical Engineering Journal, 344 (2018) 524-534.
[39] D. Ficai, A. Ficai, R. Trusca, B.S. Vasile, G. Voicu, C. Guran, E. Andronescu, Synthesis and characterization of magnetite-polysulfone micro- and nanobeads with improved chemical stability in acidic media, Current Nanoscience, 9 (2013) 271-277.
[40] J. Yin, G. Zhu, B. Deng, Graphene oxide (GO) enhanced polyamide (PA) thin-film nanocomposite (TFN) membrane for water purification, Desalination, 379 (2016) 93-101.
[41] W.J. Lau, A.F. Ismail, P.S. Goh, N. Hilal, B.S. Ooi, Characterization Methods of Thin Film Composite Nanofiltration Membranes, Separation & Purification Reviews, 44 (2015) 135-156.
[42] A.M. Dimiev, L.B. Alemany, J.M. Tour, Graphene Oxide. Origin of Acidity, Its Instability in Water, and a New Dynamic Structural Model, ACS Nano, 7 (2013) 576-588.
[43] R. Bi, Q. Zhang, R. Zhang, Y. Su, Z. Jiang, Thin film nanocomposite membranes incorporated with graphene quantum dots for high flux and antifouling property, Journal of Membrane Science, 553 (2018) 17-24.
[44] N. Melián-Martel, J.J. Sadhwani Alonso, A. Ruiz-García, Combined silica and sodium alginate fouling of spiral-wound reverse osmosis membranes for seawater desalination, Desalination, 439 (2018) 25-30.
[45] S. Lim, V.H. Tran, N. Akther, S. Phuntsho, H.K. Shon, Defect-free outer-selective hollow fiber thin-film composite membranes for forward osmosis applications, Journal of Membrane Science, 586 (2019) 281-291.
[46] S.S. Eslah, S. Shokrollahzadeh, O.M. Jazani, A. Samimi, Forward osmosis water desalination: Fabrication of graphene oxide-polyamide/polysulfone thin-film nanocomposite membrane with high water flux and low reverse salt diffusion, Separation Science and Technology, 53 (2018) 573-583.
[47] H.-g. Choi, A.A. Shah, S.-E. Nam, Y.-I. Park, H. Park, Thin-film composite membranes comprising ultrathin hydrophilic polydopamine interlayer with graphene oxide for forward osmosis, Desalination, 449 (2019) 41-49.
[48] L.M. Jin, Z.Y. Wang, S.X. Zheng, B.X. Mi, Polyamide-crosslinked graphene oxide membrane for forward osmosis, Journal of Membrane Science, 545 (2018) 11-18.